



A promising single-atom Co-N-C catalyst for efficient CO₂ electroreduction and high-current solar conversion of CO₂ to CO

Cai Wang, Houan Ren, Zihao Wang, Qingxin Guan, Yuping Liu ^{*}, Wei Li ^{*}

State Key Laboratory of Elemento-Organic Chemistry, Key Laboratory of Advanced Energy Materials Chemistry (Ministry of Education), College of Chemistry, Nankai University, Tianjin 300071, China



ARTICLE INFO

Keywords:

Single-atom Co-N-C catalyst
Electrochemical CO₂ reduction
Solar-driven electrolysis
M-N-C
DFT calculation

ABSTRACT

Excavating highly efficient M-N-C electrocatalysts for electrochemical CO₂ reduction (ECR) is of paramount importance. Herein, we report a single-atom Co-N-C catalyst (CoN₄-CB) with a high CO Faradaic efficiency (FE_{CO}, 98.7%) in ECR comparable to that of a similarly prepared NiN₄-CB catalyst. Impressively, CoN₄-CB demonstrates a CO turnover frequency of 27173 h⁻¹ and a CO current density of $-33.6 \text{ mA} \cdot \text{cm}^{-2}$ at -0.76 V , 20.2 and 6.8 times higher than that of NiN₄-CB, respectively. In a solar-driven ECR system composed of a Si solar cell and a flow cell, CoN₄-CB shows a remarkably large current density of $98.3 \text{ mA} \cdot \text{cm}^{-2}$ with an average FE_{CO} of 92.1%. Theoretical calculations suggest that the energy barrier for *COOH formation largely decreases on CoN₄ sites compared with NiN₄ sites, leading to a low onset potential and high activity for CO production. This work will boost the development of efficient M-N-C electrocatalysts and further practical application of solar-driven ECR system.

1. Introduction

The human activities such as burning coal and oil released a large amount of CO₂, which has caused serious climate and environmental issues [1,2]. Electrochemical CO₂ reduction (ECR) using renewable electricity is capable of both supplying value-added chemical feedstocks and cutting the CO₂ emission. However, this attractive approach often suffers from the stable C=O bond (806 kJ·mol⁻¹) of CO₂ and the side reaction of hydrogen evolution reaction (HER) in aqueous solutions [3]. To this end, numerous material systems, such as metals [4,5], metal oxides [6], chalcogenides [7], carbon-based nanomaterials [8], and so on, have been investigated as electrocatalysts for driving ECR. To date, developing inexpensive electrocatalysts with large current density, high selectivity and good stability operating at low overpotentials toward ECR is still a great challenge.

Recently, transition metal on nitrogen-doped carbon (M-N-C) materials, with atomically dispersed metal coordinated by N atoms (MN_x) as active sites, have demonstrated encouraging activity in ECR [9–11]. Substantial progress toward producing CO is made by using Ni, Co and Fe based M-N-C electrocatalysts, among which the Ni-N-C electrocatalysts have been widely investigated and reported owing to its stunning selectivity [12–18]. However, the Ni-N-C catalysts with NiN₄

sites still suffer the disadvantages of low CO Faraday efficiency (FE_{CO}) and CO current density at low overpotentials, which can be attributed to a high energy barrier for *COOH generation caused by the sluggish kinetics of the first coupled proton-electron transfer [19]. Previous density functional theory (DFT) calculations indicate that Co-N-C with CoN₄ sites show the more suitable energy barriers for *COOH formation and CO desorption compared with Ni-N-C [20,21], and thus it should exhibit better performance in ECR to CO. Nevertheless, most reported Co-N-C catalysts with CoN₄ sites showed poor selectivity and activity toward CO production [22–27]. Such an inconsistency between the theoretical and experimental results may be caused by the slight discrepancy between the theoretical calculation model and the actual active site. Generally, the MN₄ moiety compactly embedded in a graphitic layer is usually selected as the calculation model for M-N-C with MN₄ sites [17, 18, 28, 29], in which the nitrogen-doping type is pyridine N. But some studies have demonstrated that the nitrogen type (pyridine or pyrrole N) of MN₄ in M-N-C has a great effect on catalytic performance [30–32]. In addition, in our previous study, it was found that Co-N-C with metal-pyridine N structure exhibits higher activity than Ni-N-C with metal-pyridine N structure, while the issue of low selectivity still exists [21]. Based on the above analysis, further investigating and developing the Co-N-C catalysts with both high activity and selectivity are therefore

* Corresponding authors.

E-mail addresses: liupnk@nankai.edu.cn (Y. Liu), weili@nankai.edu.cn (W. Li).

full of importance for ECR.

Besides exploring high-performance M-N-C electrocatalysts for ECR, the utilization and integration of the renewable sunlight energy in ECR are also very essential for mitigating the energy shortage and promoting the human sustainable development. Thence, the solar-driven ECR to various value-added chemicals has attracted great attention. Several studies have demonstrated the feasibility and great prospect of producing chemicals from solar-driven ECR systems [33–36]. It is worth noting that there are few reports on solar-driven CO₂ reduction at high current density. The low solubility (approximately 30 mM) and slow diffusion of CO₂ in aqueous electrolytes limit the operation of ECR at high current density [37]. The flow cell devices with a gas-diffusion electrode (GDE) design, which have been extensively studied in recent years, can reach high current density by overcoming the mass transport limitations of CO₂ [38,39]. Accordingly, integrating the photovoltaic cell with the flow cell equipment is a promising strategy for solar-driven ECR to make a high current density viable.

Herein, we prepared a single-atom Co-N-C electrocatalyst with CoN₄ sites supported on a commercial carbon black (CoN₄-CB) by a simple method. This catalyst, as a cathodic electrocatalyst for ECR, exhibits excellent performance with a high FE_{CO} of 98.7% at -0.66 V, a CO current density of -33.6 mA·cm⁻² and a CO turnover frequency of 27173 h⁻¹ at -0.76 V, much higher than that of NiN₄-CB catalyst prepared using the same method. Furthermore, the FE_{CO} maintains over 90% for CoN₄-CB in the flow cell when the current density increases from 50 to 600 mA·cm⁻². Using the CoN₄-CB with enhanced performance as cathode, we constructed a solar-driven system for ECR by adopting a Si solar cell as power source and a flow cell device as the electrochemical reactor. The combined system demonstrates a remarkably high current density of 98.3 mA·cm⁻² with an average FE_{CO} of 92.1% and a solar-to-CO conversion efficiency of approximately 4.9%. Based on the nitrogen type in MN₄ sites is pyridine N, DFT calculations reveal that CoN₄ sites greatly accelerate the rate-limiting step of *COOH generation compared with NiN₄ sites, and thus facilitate the CO production.

2. Experimental section

2.1. Chemicals

All reagents were directly used without extra purification. 1,10-phenanthroline was obtained from Ark Pharm Co. Ltd. Cobalt acetate tetrahydrate and Nickel acetate tetrahydrate were purchased from Heowns Co. Ltd. Nafion solution (5 wt%) and Nafion 117 membrane were acquired from Sigma-Aldrich.

2.2. Synthesis of catalysts

0.024 mmol of cobalt (II) acetate tetrahydrate and 0.072 mmol of 1,10-phenanthroline were dissolved in 3 mL of ethanol and stirred at 323 K for 3 h to acquire the Co-phen complex. Then 60 mg of carbon black (Vulcan XC-72R) was mixed with the above complex solution and stirred at 323 K for 3 h, followed by evaporation drying at 353 K. The obtained mixture was pyrolyzed at 923 K (10 K·min⁻¹) and maintained for 2 h at an argon atmosphere (100 mL·min⁻¹). The black products were immersed into 0.5 M HCl for 12 h at 353 K and washed with water to obtain CoN₄-CB. NiN₄-CB was prepared under the same procedure except that cobalt acetate tetrahydrate was replaced by nickel acetate tetrahydrate.

2.3. Electrochemical measurements

For the preparation of the catalyst inks, 5 mg of catalysts were dispersed in 0.98 mL ethanol, and then mixed with 20 μ L of nafion solution. The catalyst inks were sonicated for 60 min to ensure uniform mixing. Subsequently, the 100 μ L of as-prepared ink was dropped onto a

1 \times 1 cm² carbon paper and then dried in a vacuum oven at 343 K for 12 h. The resulting catalyst loading at each working electrode was 0.5 mg·cm⁻². For the flow cell, 20 μ L Nafion solution, 5 mg of carbon black and 5 mg of catalysts were mixed with 0.98 mL mixture (ethanol and water with a volume ratio of 3:1), and sonicated for at least 60 min. Then 200 μ L of ink was deposited on a carbon gas-diffusion layer (1 \times 1 cm²) with a catalyst loading of 1 mg·cm⁻².

In H-type cell, the electrochemical measurements were carried out in CO₂-saturated 0.5 M KHCO₃ aqueous solution (pH = 7.2) using Ag/AgCl (saturated KCl) electrode as reference electrode and Pt sheet as counter electrode. A sheet of Nafion 117 membrane was employed to separate the cathode compartment and anode compartment. All the potentials were calibrated to a reversible hydrogen electrode (RHE) according to the Nernst equation ($E_{(RHE)} = E_{(Ag/AgCl)} + 0.0591 \times pH + 0.21$). The linear sweep voltammetry (LSV) was carried out in CO₂- or Ar-saturated 0.5 M KHCO₃ electrolyte with a scan rate of 20 mV·s⁻¹. The KHCO₃ solution was purged with CO₂ for 30 min before the measurement. Chronoamperometry (CA) was adopted to evaluate the ECR performance of catalysts under different potentials.

For the flow cell measurements, catalyst-supported GDE, nickel foam and Ag/AgCl (saturated KCl) electrode were employed as cathode, anode and reference electrode, respectively. An anionic exchange membrane (AEM) was interposed between anolyte and catholyte chamber. 1 M KOH solution as catholyte was circulated in cathode chamber by means of a peristaltic pump with a constant flow of 5 mL·min⁻¹. In addition, the anolyte (1 M KOH) was quickly circulated through anode chamber by using a specially-made gas-liquid mixed flow pump. High purity CO₂ was purged in the catholyte chamber under a constant flow of 28 mL·min⁻¹. The performance of electrocatalysts in ECR at various current densities were evaluated by the chronopotentiometry (CP).

The gas products of ECR were monitored by an online gas chromatography (GC) equipped (FULI 9790) with a TCD detector once every 14 min. The liquid products were analyzed and quantified through a Bruker AVANCE III 400 MHz nuclear magnetic resonance (NMR) spectrometer.

2.4. Solar-Driven CO₂ Electroreduction

Solar-driven ECR experiments were performed in a flow cell with CoN₄-CB and Ni foam as cathode and anode, respectively. A commercially available a-Si photovoltaic cell (5 cm \times 5 cm) as a light absorber is used to drive the system. To simulate the solar light illumination, the intensity of incident light was calibrated at 100 mW·cm⁻² by a Si photodiode (Thorlabs, Inc.), from a 300 W Xenon arc lamp (Beijing Perfectlight Technology Co. Ltd., PLS-SXE 300 + UV) accompanied with an AM 1.5 G filter. The current-voltage curve of the solar cell under the simulated AM 1.5 G light was measured by a source meter (Keithley 2450 SourceMeter SMU). At the maximum power point, the voltage and current were 2.95 V and 100.98 mA, respectively, showing a maximum efficiency of 11.9% under 1 sun irradiation. The testing conditions and product analysis in solar-driven ECR system are same as the mentioned above in Electrochemical measurements.

3. Results and discussion

3.1. Catalyst Synthesis and characterization

The synthesis of MN₄-CB (M = Co or Ni) electrocatalysts is schematically shown in Fig. 1a. In brief, carbon black and metal 1,10-phenanthroline complex (M-phen, M = Co or Ni) were well mixed and pyrolyzed at 923 K for 2 h under Ar atmosphere, followed by acid leaching in HCl. The catalyst synthesis is based on a universal ligand mediated method for transition metal single atom catalysts [40]. Transmission electron microscopy (TEM) images of CoN₄-CB and NiN₄-CB verify that no metal nanoparticles were observed on the carbon frame (Fig. 1b and Fig.S1a). And the elemental mapping analyses

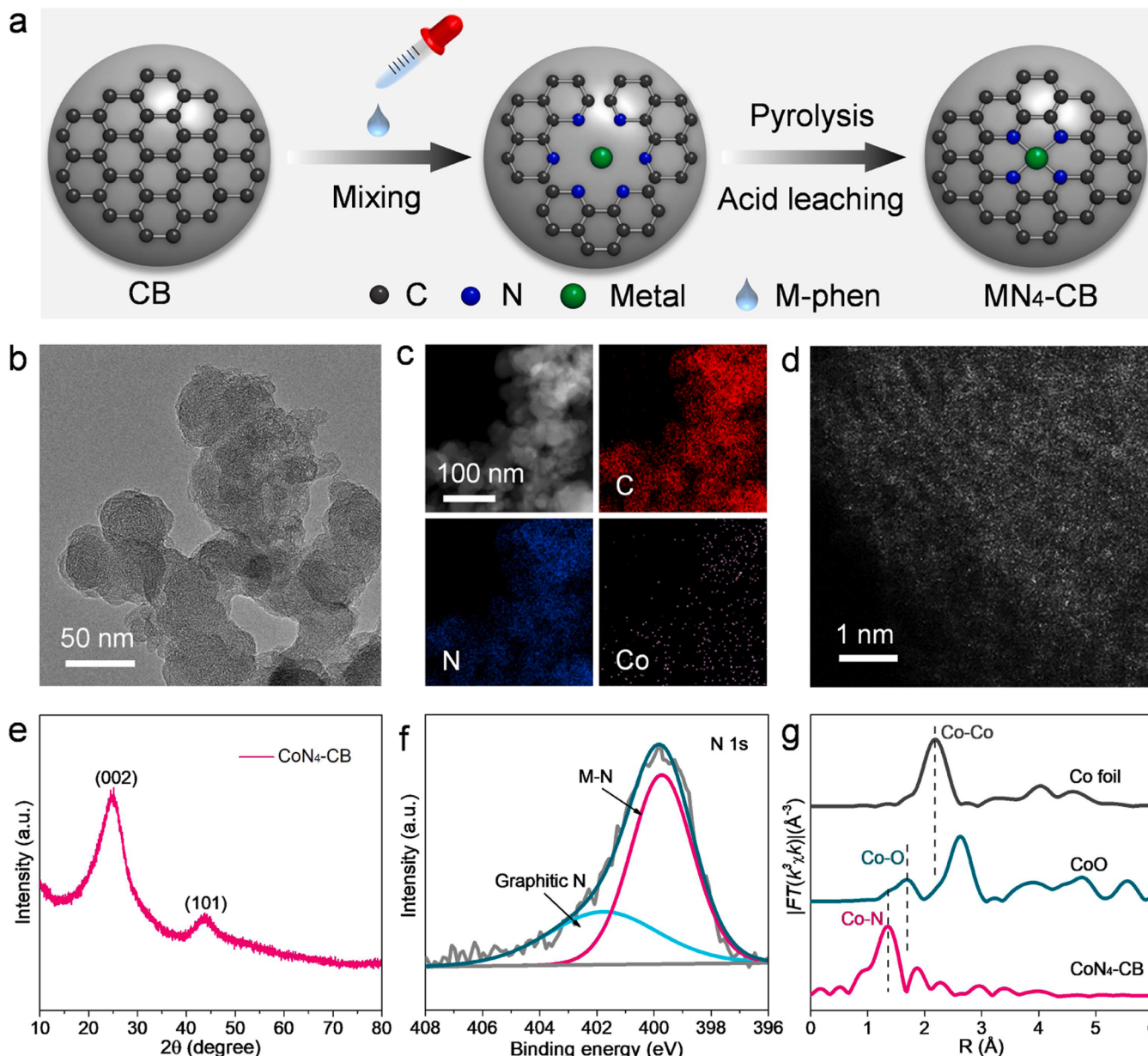


Fig. 1. (a) Schematic illustration of MN_4 -CB preparation. (b) TEM image, (c) elemental mapping, (d) HAADF-STEM image, (e) XRD pattern, (f) N 1s XPS, and (g) Fourier-transform EXAFS spectra of CoN_4 -CB.

confirm the homogeneous dispersion of Co or Ni elements over the nitrogen-doped carbon support (Fig. 1c and Fig. S1b). The brighter spots in Fig. 1d and Fig. S1c further confirm the well dispersed metal atoms rather than metal clusters on the carbon support. Furthermore, X-ray diffraction (XRD) patterns of both samples show only two main peaks corresponding to the (002) and (101) planes of graphite (JCPDS NO. 75-1621) [15,20], and no metallic phases exist (Fig. 1e and Fig. S1d).

X-ray photoelectron spectroscopy (XPS) analysis was conducted to investigate the chemical information of CoN_4 -CB and NiN_4 -CB (Fig. S2 and Table S1). The N 1 s high-resolution spectra for both samples exhibit two characteristic peaks, corresponding to metal-N (M-N) and graphitic N (Fig. 1f and Fig. S1e). The metal 2p XPS spectra of MN_4 -CB show a peak of $Co2p_{3/2}$ at 780.8 eV and a peak of $Ni2p_{3/2}$ at 855.7 eV (Fig. S3), which can be ascribed to the chemical states of Co^{2+} and Ni^{2+} , respectively [41]. Furthermore, the local environment of metal atoms was explored by X-ray absorption near-edge structure (XANES) and extended X-ray absorption fine structure (EXAFS) analyses. The Co K-edge XANES

spectrum show that the oxidation state of Co in CoN_4 -CB is between 0 and 2+ (Fig. S4a), as compared with Co foil and CoO. Concurrently, the Ni K-edge XANES spectrum of NiN_4 -CB shows that the oxidation state of Ni in NiN_4 -CB is between 0 and 2+ (Fig. S4b), as compared with Ni foil and NiO. The derivative of corresponding XANES curves further confirms that the oxidation states of Co and Ni both approach 2+ (Fig. S5), which are consistent with the results of XPS analysis. The EXAFS spectrum of CoN_4 -CB at Co K-edge exhibits an obvious peak at around 1.35 Å (Fig. 1g), which can be attributed to the existence of Co-N bond. The main peak position of Co-N is quite different from that of the relevant reference samples, indicating no existence of Co-Co and Co-O bonds in CoN_4 -CB. The collected EXAFS data for NiN_4 -CB are similar to the analysis for CoN_4 -CB, providing evidence for the existence of Ni-N bond in NiN_4 -CB (Fig. S1f). The EXAFS fitting results reveal that the metal atom in MN_4 -CB were mainly coordinated by four N atoms with the form of MN_4 (Fig. S6 and Table S2). Accordingly, the combined characterization results from HAADF-STEM, XPS, XANES and XAFS

demonstrate MN_4 -CB possess a single metal atom configuration with four N coordination.

3.2. Performance evaluation for ECR

The catalytic performance of two samples toward ECR was first evaluated in the H-cell containing CO_2 -saturated 0.5 M $KHCO_3$ electrolyte. LSV curves of the MN_4 -CB electrocatalysts exhibit a lower onset potential than that of CB sample without metal doping, with the order of CoN_4 -CB < NiN_4 -CB < CB (Fig. 2a). In addition, CoN_4 -CB shows much larger current density ($-55.5\text{ mA}\cdot\text{cm}^{-2}$) than that of NiN_4 -CB ($-16.2\text{ mA}\cdot\text{cm}^{-2}$) at -0.9 V . The results from LSV indicate the remarkable activity of CoN_4 -CB for ECR. Chronoamperometric electrolysis was applied to detect the products in CO_2 reduction with the help of online GC and NMR spectroscopy (Fig. S7). H_2 and CO are the only products, and liquid products are not detected (Fig. S8). As shown in Fig. 2b, CoN_4 -CB shows a lower onset potential (-0.36 V) toward ECR than that of NiN_4 -CB (-0.56 V). What's more, at a potential of -0.56 V , NiN_4 -CB exhibits a CO Faradaic efficiency (FE_{CO}) of 59.3%, while FE_{CO} of CoN_4 -CB is up to 90.7% (Fig. 2b). NiN_4 -CB achieves a maximum FE_{CO} of 99.1% at -0.86 V , the excellent selectivity of single-atom Ni-N-C electrocatalysts for CO production has also been observed in many

reports [14,16–18]. However, CoN_4 -CB can also achieve a comparable selectivity for CO production (with maximum FE_{CO} of 98.7%) at lower potential (-0.66 V) as compared with NiN_4 -CB. Concurrently, CoN_4 -CB displays lower selectivity for H_2 production than that of NiN_4 -CB at low potential (Fig. S9). More importantly, despite similar FE_{CO} of the NiN_4 -CB (96.2%) and CoN_4 -CB (97.5%) exhibited at -0.76 V , the CO current density (j_{CO}) on CoN_4 -CB reaches $-33.6\text{ mA}\cdot\text{cm}^{-2}$, 6.8 times as high as that of NiN_4 -CB ($-4.9\text{ mA}\cdot\text{cm}^{-2}$) (Fig. 2c). What's more, CoN_4 -CB exhibits much outstanding turnover frequency (TOF) of CO compared with NiN_4 -CB in the applied potential range (Fig. 2d). Specifically, the CO TOF of CoN_4 -CB reaches 27173 h^{-1} at -0.76 V , about 20.2 times higher than that calculated for NiN_4 -CB (1348 h^{-1}). These results indicate that performance of CoN_4 -CB for CO production exceeds that of NiN_4 -CB. In addition, the high performance (high activity and selectivity at low overpotentials) of CoN_4 -CB for ECR to CO in H-type cell is comparable to or exceeds some state-of-the-art electrocatalysts (Table S3).

The long-term chronopotentiometry was adopted to evaluate the stability of CoN_4 -CB and NiN_4 -CB. Both catalysts can maintain over 14-h electrolysis tests under a constant current density of $-15\text{ mA}\cdot\text{cm}^{-2}$. During the electrolysis, the potential of CoN_4 -CB remains stable at about -0.62 V , while the potential of NiN_4 -CB declines from -0.91 V to

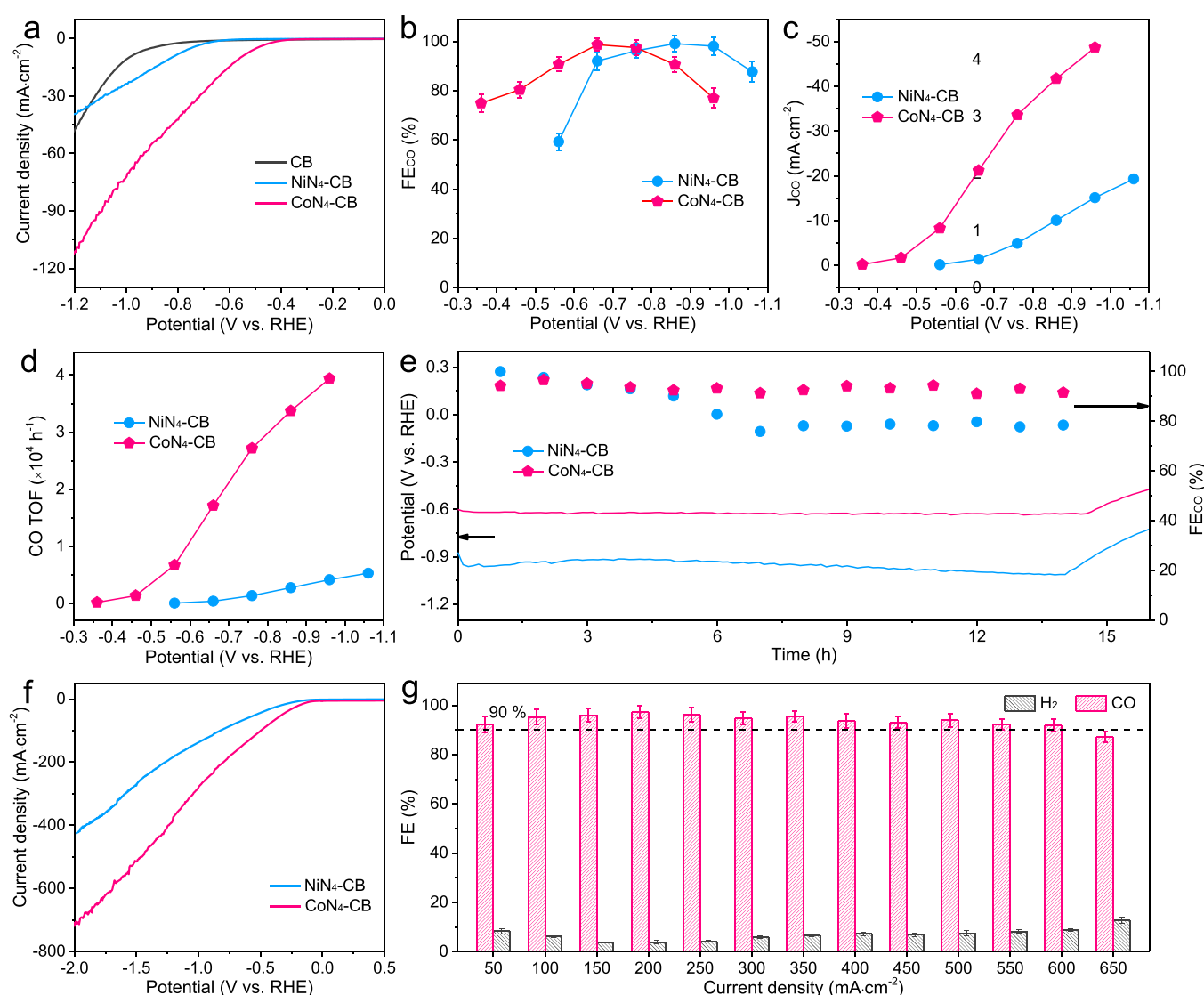


Fig. 2. (a) LSV curves of CB, NiN_4 -CB and CoN_4 -CB in the H-type cell. (b) FE_{CO} , (c) j_{CO} , (d) CO TOF, and (e) long-term stability tested at $-15\text{ mA}\cdot\text{cm}^{-2}$ for NiN_4 -CB and CoN_4 -CB. (f) LSV curves of NiN_4 -CB and CoN_4 -CB in the flow cell. (g) FE for CO and H_2 of CoN_4 -CB at different current densities in the flow cell.

– 1.0 V (Fig. 2e). Correspondingly, the FE_{CO} of $\text{CoN}_4\text{-CB}$ is well maintained above 90%, and instead there is a marked decline in the FE_{CO} of $\text{NiN}_4\text{-CB}$ from 99.8% to 78.4%. After the 14-h stability test, the characterization results of $\text{CoN}_4\text{-CB}$ show that the chemical/coordination states of Co (Fig. S10) and the morphology of catalysts with uniform elemental distribution and high atomic dispersion (Fig. S11) well retain, further indicating the catalytic stability of $\text{CoN}_4\text{-CB}$. The stability tests reveal that $\text{CoN}_4\text{-CB}$ possesses superior stability compared with $\text{NiN}_4\text{-CB}$ at low potential, which may be due to the good resistance to demetallation of Co-N-C catalysts [30].

Generally, due to the limited low solubility of CO_2 in aqueous solutions, it is difficult for ECR to achieve a high industrial current density in the conventional H-type cell [39]. Therefore, a flow device equipped with a GDE was applied to overcome the low solubility of CO_2 and enhance the mass transfer process [37]. The larger current density obtained from the flow cell as compared with H cell demonstrates the advantage of the flow device (Fig. 2a and Fig. 2f). In particular, LSV curves measured in the flow cell show a higher current density for $\text{CoN}_4\text{-CB}$ than for $\text{NiN}_4\text{-CB}$ at the same applied potential (Fig. 2f). For $\text{CoN}_4\text{-CB}$, as the current density increases from 50 to $600 \text{ mA}\cdot\text{cm}^{-2}$ (Fig. 2g), the FE_{CO} reaches over 90% and only a small amount of H_2 is produced. However, for $\text{NiN}_4\text{-CB}$, such an FE_{CO} of over 90% can only be reached at relatively low current density range ($50\text{--}250 \text{ mA}\cdot\text{cm}^{-2}$), and a larger current density ($> 250 \text{ mA}\cdot\text{cm}^{-2}$) leads to a sharp drop in FE_{CO} owing to the enhanced HER (Fig. S12). It is worth noting that the enhanced performance of $\text{CoN}_4\text{-CB}$ for CO_2 -to-CO conversion in the flow cell observed here exceeds those of almost all state-of-the-art ECR electrocatalysts including single-atom, molecular, noble-metal, metallic oxide, and carbon-supported metal nanoparticles electrocatalysts (Table S4).

3.3. Solar-driven ECR

As mentioned above, $\text{CoN}_4\text{-CB}$ exhibits enhanced performance

toward ECR with an outstanding selectivity for CO products within a wide current density range in the flow cell. On this basis, we attempt to select it as a cathode for the solar-driven ECR (SDECR) system. As shown in Fig. 3a, the proposed SDECR system is composed of a flow cell and a commercially available a-Si photovoltaic cell (PV cell, $5 \text{ cm} \times 5 \text{ cm}$, Fig. S13), where solar light is the only energy input. Under standard AM 1.5 G solar light with the intensity of $100 \text{ mW}\cdot\text{cm}^{-2}$ (1 sun), the Si solar cell shows an open-circuit voltage (V_{OC}) of 3.51 V and a short circuit current of about 103 mA (see the blue line in Fig. 3b). The position of maximum power point (MPP) of the solar cell is obtained by multiplying the current and voltage, and marked as a gray star in Fig. 3b, the maximum output voltage (2.95 V) is enough high to drive ECR.

The intersection of current-voltage profile of the solar cell with LSV curve of flow cell is very close to the MPP, indicating that the integrated system can run well with an optimized condition [33,34]. According to the intersection point, the operating voltage and current are determined to be 2.99 V and 99.22 mA, respectively. Under the operating conditions, the $\text{CoN}_4\text{-CB}$ achieved an average FE_{CO} of 92.1% at a large current density of about $98.4 \text{ mA}\cdot\text{cm}^{-2}$ during the 4 h test period (Fig. 3c), reflecting the superior performance and good stability of $\text{CoN}_4\text{-CB}$ in the integrated SDECR system. Moreover, the average solar-to-CO conversion efficiency reaches about 4.9% (Fig. S14). Table S5 shows some previous studies about CO_2 conversion to CO in the SDECR system, and few systems are able to convert solar energy into CO under such a high current density. To further demonstrate the superiority of the system of combining the solar cell with the flow cell, the same tests in traditional H-type cell were conducted. The intersection of the LSV curve from the H-type cell with the current-voltage profile of the solar cell locates at 3.47 V with a current of 9.4 mA (Fig. S15), which is far from the MPP of the Si solar cell. Therefore, it is no doubt that a small current density and a low solar-to-CO conversion efficiency will be obtained in the H-type cell.

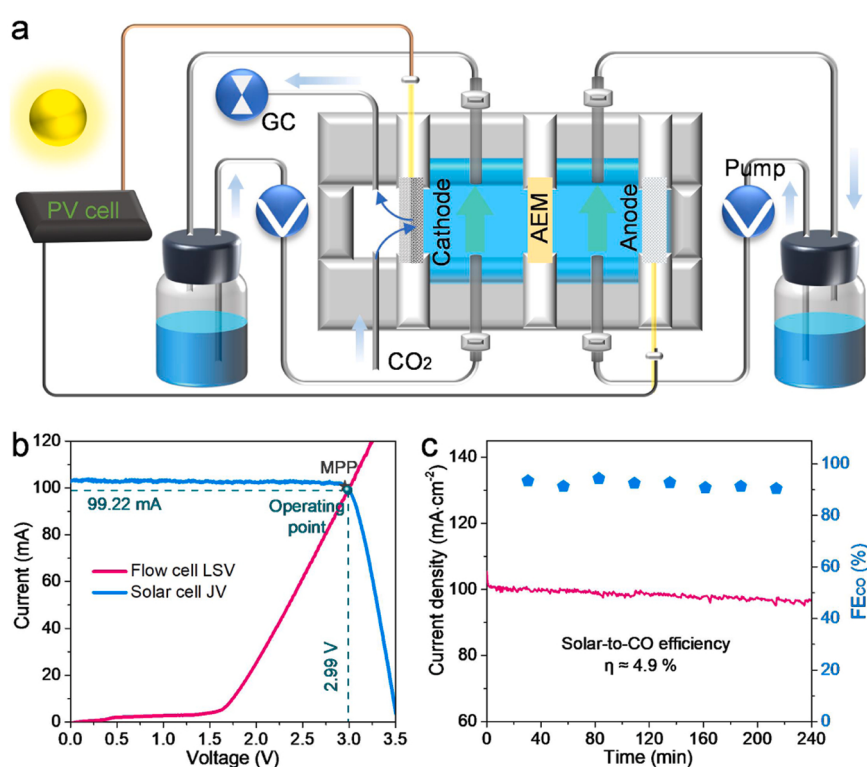


Fig. 3. (a) Schematic illustration of the SDECR system. The surface area of the anode (Ni mesh) and cathode are all 1 cm^2 . (b) Current-potential curve of photovoltaic cell at 1 sun illumination (blue line) and tested working current of the flow cell (pink line). (c) The stability test of $\text{CoN}_4\text{-CB}$ in SDECR system. (For interpretation of the references to color in this figure legend, the reader is referred to the web version of this article.)

3.4. Mechanism investigation

To understand the electrokinetic mechanism of ECR on $\text{MN}_4\text{-CB}$, Tafel analyses and electrochemical impedance spectroscopy (EIS) tests were carried out. The Tafel slope of $\text{CoN}_4\text{-CB}$ ($118.1 \text{ mV}\cdot\text{dec}^{-1}$) is lower than that of $\text{NiN}_4\text{-CB}$ ($148.9 \text{ mV}\cdot\text{dec}^{-1}$), demonstrating the higher kinetic activity of $\text{CoN}_4\text{-CB}$ for CO production (Fig. 4a). Moreover, the Tafel slope is closed to $118 \text{ mV}\cdot\text{dec}^{-1}$, suggesting that the formation of the COOH^* intermediate via the first electron-proton coupling process is the rate-determining step [39,41]. The EIS show a much smaller radius in $\text{CoN}_4\text{-CB}$ as compared with that of $\text{NiN}_4\text{-CB}$ (Fig. 4b), indicating a faster charge transfer rate, and thus resulting in a high current density. In addition, LSV curves in Fig. S16 show that $\text{CoN}_4\text{-CB}$ possesses a high current density under both Ar- and CO_2 -saturated 0.5 M KHCO_3 solution, indicating its superior electrical conductivity. Finally, electrochemical capacitance tests were adopted to assess the electrochemical active surface area (ECSA) of both catalysts (Fig. S17). After normalizing to ECSA, the higher CO current density of $\text{CoN}_4\text{-CB}$ than that of $\text{NiN}_4\text{-CB}$ again demonstrates its enhanced performance for ECR to CO (Fig. 4c).

Moreover, among numerous studies on the Co-N-C electrocatalysts with CoN_4 sites for ECR (Table S6), it can be found that the maximum FE_{CO} varies between 5% and 98.5% with a corresponding j_{CO} in the range of $0.8\text{--}16 \text{ mA}\cdot\text{cm}^{-2}$. And $\text{CoN}_4\text{-CB}$ in our work shows excellent performance with a high FE_{CO} of 98.7% and a j_{CO} of $21.2 \text{ mA}\cdot\text{cm}^{-2}$ at -0.66 V . In fact, different local coordination structures may lead to the diverse catalytic performance [42]. Specifically, though the active centers are all CoN_4 sites, the effect of the nitrogen type in the CoN_4 sites on the catalytic performance can't be ignored. For example, Wang and co-workers [43] reported two cobalt complex catalysts with CoN_4 sites, the Co(II)CPY/CNT (the type of coordination nitrogen is pyridine N) exhibited higher selectivity and activity than the Co-TPP/CNT (the type of coordination nitrogen is pyrrole N). Therefore, it is necessary to confirm the type of coordination nitrogen in $\text{MN}_4\text{-CB}$. Three reference samples, 1,10-phenanthroline (Phen), metal meso-tetraphenylporphyrin (MTPP, M = Co, Ni) with M-pyrrole N structure and metal 1,10-phenanthroline complex (M-phen, M = Co, Ni) with M-pyridine N structure, are selected to compare with the $\text{MN}_4\text{-CB}$ catalysts. Fig. S18 shows that the peaks at around 399.7 eV ($\text{CoN}_4\text{-CB}$) and 399.4 eV ($\text{NiN}_4\text{-CB}$) can be

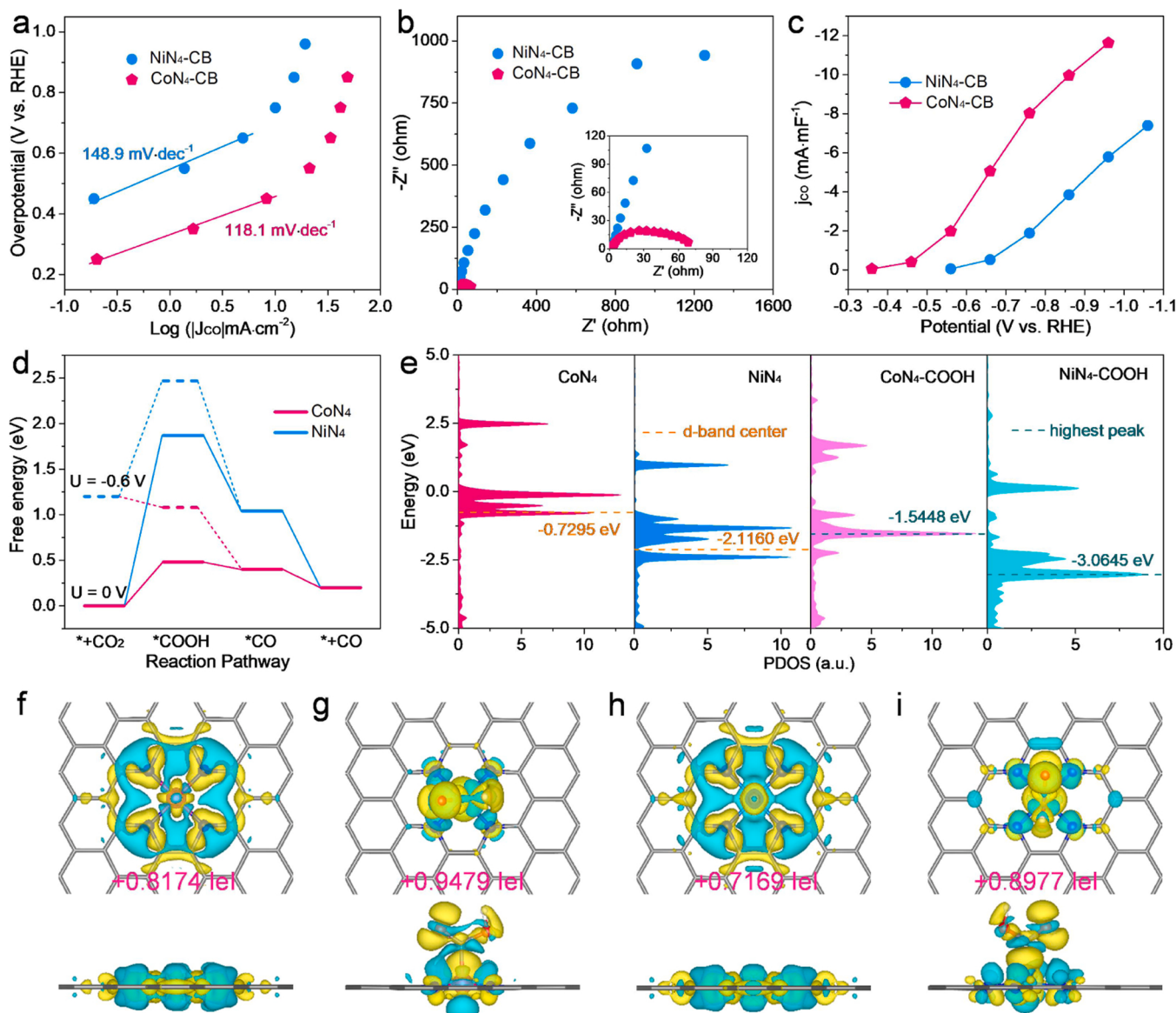


Fig. 4. (a) Tafel plots, (b) EIS spectra, and (c) normalized j_{CO} based on the ECSA of $\text{NiN}_4\text{-CB}$ and $\text{CoN}_4\text{-CB}$. (d) Gibbs free energy diagrams for ECR to CO over CoN_4 and NiN_4 sites. (e) The PDOS of CoN_4 , NiN_4 , $\text{CoN}_4\text{-COOH}$ and $\text{NiN}_4\text{-COOH}$. Charge density difference of (f) CoN_4 , (g) $\text{CoN}_4\text{-COOH}$, (h) NiN_4 , and (i) $\text{NiN}_4\text{-COOH}$; cyan and yellow areas donate the aggregation and dissipation of electrons, respectively.

assigned to pyridinic-N coordinated to metal, such a N configuration is in line with M-phen and other previous reports [12,19,20,44].

DFT calculations were performed to further explore the mechanism for the enhanced performance of CoN_4 -CB on ECR. Based on the above analysis and structural characterizations obtained in this work, CoN_4 and NiN_4 moiety anchored on a graphitic layer are proposed as potential site candidates for MN_4 -CB catalysts, in which the coordination nitrogen is pyridine N. The pathway of ECR to CO involves the generation of COOH^* and CO^* intermediates according to the coupled proton-electron transfer process reported by previous studies [45]. Fig. 4d shows an increased formation energy for COOH^* on CoN_4 and NiN_4 at an electrode potential of 0 V, and the free energy gap of CoN_4 -CB (0.48 eV) is lower than that of NiN_4 -CB (1.87 eV), suggesting that CoN_4 -CB is more favorable for CO_2 reduction. Notably, as an electrode potential of -0.6 V is applied, NiN_4 -CB still displays an uphill energy for ${}^*\text{COOH}$ generation, whereas CoN_4 -CB exhibits a downhill energy for ${}^*\text{COOH}$ generation, indicating a lower onset potential for CO formation of CoN_4 -CB than that of NiN_4 -CB [23,46], which is in line with our experimental results. It is well known that during the ECR process, HER is inevitable as a competitive reaction (Fig. S19a). A slight difference value of the limiting potentials between ECR and HER suggests a good selectivity to CO for CoN_4 -CB and NiN_4 -CB (Fig. S19b). Next, the metal 3d partial density of state (PDOS) and charge density difference were calculated to analyze the electronic properties of CoN_4 and NiN_4 , which further provide the intrinsic elucidation. The plots of PDOS (Fig. 4e) show that the position of d-band center of CoN_4 is much closer to Fermi level than that of NiN_4 , which could promote the electron transfer and further strengthen the binding interaction of ${}^*\text{COOH}$ intermediate on CoN_4 [29]. Additionally, after adsorbing COOH^* intermediates, the position of the highest peak of CoN_4 is also closer to Fermi level than that of NiN_4 , further signifying a higher adsorption strength of CoN_4 for ${}^*\text{COOH}$ [39]. Differential charge graphs display the charge distribution in CoN_4 (Fig. 4f), NiN_4 (Fig. 4g), CoN_4 -COOH (Fig. 4h) and NiN_4 -COOH (Fig. 4i). There exists an obvious electron transfer in metal-C bonding area between $\text{CoN}_4/\text{NiN}_4$ and ${}^*\text{COOH}$, and more electron density accumulation areas exist between CoN_4 and ${}^*\text{COOH}$, leading to an enhanced binding strength with the adsorbed ${}^*\text{COOH}$, thus effectively adjusting the reaction energy barrier. Simultaneously, after interacting with ${}^*\text{COOH}$, the charge of Co atom in CoN_4 shows a smaller increase of 0.1305 $|\epsilon|$ than that of Ni atom in NiN_4 (0.1808 $|\epsilon|$), indicating that the Co atom only needs to transfer fewer electrons to surroundings than the Ni atom from MN_4 sites to MN_4 -COOH structure. That is to say, CoN_4 can more easily accelerate the first coupled proton-electron transfer and bring about a lower energy barrier for ${}^*\text{COOH}$ generation than NiN_4 , and then decreasing the onset potential.

4. Conclusions

In conclusion, we have developed a single-atom Co-N-C electrocatalyst with typical CoN_4 sites for efficient ECR. The CoN_4 -CB catalyst shows a maximum FE_{CO} of 98.7% at -0.66 V, and reaches much higher FE_{CO} (90.7%) than that of NiN_4 -CB (59.3%) under a low potential of -0.56 V. More importantly, the j_{CO} and CO TOF on CoN_4 -CB reach $-33.6 \text{ mA} \cdot \text{cm}^{-2}$ and 27173 h^{-1} , 6.8 and 20.2 times higher than that of NiN_4 -CB at -0.76 V, respectively. In addition, CoN_4 -CB exhibits a high FE_{CO} over 90% in the flow cell under a wide current density ranging from 50 to $600 \text{ mA} \cdot \text{cm}^{-2}$. The enhanced performance in ECR of CoN_4 -CB enables it as a cathode for the SDECR system, which can be driven by a Si solar cell coupled with a flow cell device under the simulated AM 1.5 G illumination. CoN_4 -CB achieves a much high current density of $98.3 \text{ mA} \cdot \text{cm}^{-2}$ and an average FE_{CO} of 92.1% in the combined system. Electrochemical characterizations and theoretical calculations reveal that CoN_4 -CB possesses exclusive electrochemical property and electronic structures, which is favorable to decrease the energy barrier for the key intermediate (${}^*\text{COOH}$) formation, leading to a low onset potential for ECR. Our work deeply investigates a single-atom Co-N-C

catalyst with enhanced performance in ECR, which is full of significance to the development of M-N-C catalyst toward ECR. Concurrently, the proposed optimized SDECR system enables the industrial possibility of CO_2 electroreduction for CO production at a high current density.

CRediT authorship contribution statement

Cai Wang: Conceptualization, Methodology, Software, Data curation, Writing – original draft preparation, Writing - review & editing, **Houan Ren:** Investigation, **Zihao Wang:** Investigation, **Qingxin Guan:** Methodology, **Yuping Liu:** Writing - review & editing, **Wei Li:** Resources, Supervision, Funding acquisition, Writing - review & editing.

Declaration of Competing Interest

The authors declare that they have no known competing financial interests or personal relationships that could have appeared to influence the work reported in this paper.

Acknowledgements

This work was supported by the National Natural Science Foundation of China (NSFC 21878162 and 21978137). The authors would like to thank Jiayan Xue from Shiyanjia Lab (www.shiyanjia.com) for the XPS analysis. This work is dedicated to the 100th anniversary of Chemistry at Nankai University.

Appendix A. Supporting information

Supplementary data associated with this article can be found in the online version at doi:10.1016/j.apcatb.2021.120958.

References

- [1] S. Lin, C.S. Diercks, Y.B. Zhang, N. Kornienko, E.M. Nichols, Y. Zhao, A.R. Paris, D. Kim, P. Yang, O.M.J.S. Yaghi, Covalent organic frameworks comprising cobalt porphyrins for catalytic CO_2 reduction in water, *Science* 349 (2015) 1208–1213, <https://doi.org/10.1126/science.aac8343>.
- [2] D.-D. Ma, S.-G. Han, C. Cao, X. Li, X.-T. Wu, Q.-L. Zhu, Remarkable electrocatalytic CO_2 reduction with ultrahigh CO/H_2 ratio over single-molecularly immobilized pyrrolidinonyl nickel phthalocyanine, *Appl. Catal. B Environ.* 264 (2020), 118530, <https://doi.org/10.1016/j.apcatb.2019.118530>.
- [3] W. Ni, Z. Liu, Y. Zhang, C. Ma, H. Deng, S. Zhang, S. Wang, Electroreduction of carbon dioxide driven by the intrinsic defects in the carbon plane of a single Fe-N_4 site, *Adv. Mater.* 33 (2021), 2003238, <https://doi.org/10.1002/adma.202003238>.
- [4] D. Kim, C. Xie, N. Becknell, Y. Yu, M. Karamad, K. Chan, E.J. Crumlin, J. K. Norskov, P. Yang, Electrochemical activation of CO_2 through atomic ordering transformations of AuCu nanoparticles, *J. Am. Chem. Soc.* 139 (2017) 8329–8336, <https://doi.org/10.1021/jacs.7b03516>.
- [5] L. Peng, Y. Wang, Y. Wang, N. Xu, W. Lou, P. Liu, D. Cai, H. Huang, J. Qiao, Separated growth of Bi-Cu bimetallic electrocatalysts on defective copper foam for highly converting CO_2 to formate with alkaline anion-exchange membrane beyond KHCO_3 electrolyte, *Appl. Catal. B Environ.* 288 (2021), 120003, <https://doi.org/10.1016/j.apcatb.2021.120003>.
- [6] W. Luo, Q. Zhang, J. Zhang, E. Moioli, K. Zhao, A. Züttel, Electrochemical reconstruction of ZnO for selective reduction of CO_2 to CO, *Appl. Catal. B Environ.* 273 (2020), 119060, <https://doi.org/10.1016/j.apcatb.2020.119060>.
- [7] J. Xu, X. Li, W. Liu, Y. Sun, Z. Ju, T. Yao, C. Wang, H. Ju, J. Zhu, S. Wei, Y. Xie, Carbon dioxide electroreduction into syngas boosted by a partially delocalized charge in molybdenum sulfide selenide alloy monolayers, *Angew. Chem. Int. Ed.* 56 (2017) 9121–9125, <https://doi.org/10.1002/anie.201704928>.
- [8] F. Pan, B. Li, W. Du, Y. Gang, G. Wang, Y. Li, Promoting electrocatalytic CO_2 reduction on nitrogen-doped carbon with sulfur addition, *Appl. Catal. B Environ.* 252 (2019) 240–249, <https://doi.org/10.1016/j.apcatb.2019.04.025>.
- [9] C. Liu, Y. Wu, K. Sun, J. Fang, A. Huang, Y. Pan, W.-C. Cheong, Z. Zhuang, Z. Zhuang, Q. Yuan, H.L. Xin, C. Zhang, J. Zhang, H. Xiao, C. Chen, Y. Li, Constructing FeN_4 /graphitic nitrogen atomic interface for high-efficiency electrochemical CO_2 reduction over a broad potential window, *Chem* 7 (2021) 1297–1307, <https://doi.org/10.1016/j.chempr.2021.02.001>.
- [10] S.G. Han, D.D. Ma, S.H. Zhou, K. Zhang, W.B. Wei, Y. Du, X.T. Wu, Q. Xu, R. Zou, Q.-L. Zhu, Fluorine-tuned single-atom catalysts with dense surface Ni-N_4 sites on ultrathin carbon nanosheets for efficient CO_2 electroreduction, *Appl. Catal. B Environ.* 283 (2021), <https://doi.org/10.1016/j.apcatb.2020.119591>.
- [11] X. Rong, H.J. Wang, X.L. Lu, R. Si, T.B. Lu, Controlled synthesis of a vacancy-defect single-atom catalyst for boosting CO_2 electroreduction, *Angew. Chem. Int. Ed.* 59 (2020) 1961–1965, <https://doi.org/10.1002/anie.201912458>.

[12] J.H. Guo, W.Y. Sun, Integrating nickel-nitrogen doped carbon catalyzed CO_2 electroreduction with chlor-alkali process for CO , Cl_2 and KHCO_3 production with enhanced techno-economics, *Appl. Catal. B-Environ.* 275 (2020), 119154, <https://doi.org/10.1016/j.apcatb.2020.119154>.

[13] K. Mou, Z. Chen, X. Zhang, M. Jiao, X. Zhang, X. Ge, W. Zhang, L. Liu, Highly efficient electroreduction of CO_2 on nickel Single-atom catalysts: atom trapping and nitrogen anchoring, *Small* 15 (2019), 1903668, <https://doi.org/10.1002/smll.201903668>.

[14] C. Yan, H. Li, Y. Ye, H. Wu, F. Cai, R. Si, J. Xiao, S. Miao, S. Xie, F. Yang, Y. Li, G. Wang, X. Bao, Coordinatively unsaturated nickel-nitrogen sites towards selective and high-rate CO_2 electroreduction, *Energy Environ. Sci.* 11 (2018) 1204–1210, <https://doi.org/10.1039/c8ee00133b>.

[15] P. Lu, Y. Yang, J. Yao, M. Wang, S. Dipazir, M. Yuan, J. Zhang, X. Wang, Z. Xie, G. Zhang, Facile synthesis of single-nickel-atomic dispersed N-doped carbon framework for efficient electrochemical CO_2 reduction, *Appl. Catal. B-Environ.* 241 (2019) 113–119, <https://doi.org/10.1016/j.apcatb.2018.09.025>.

[16] Y. Hou, Y.-L. Liang, P.-C. Shi, Y.-B. Huang, R. Cao, Atomically dispersed Ni species on N-doped carbon nanotubes for electroreduction of CO_2 with nearly 100% CO selectivity, *Appl. Catal. B-Environ.* 271 (2020), <https://doi.org/10.1016/j.apcatb.2020.118929>.

[17] H.B. Yang, S.-F. Hung, S. Liu, K. Yuan, S. Miao, L. Zhang, X. Huang, H.-Y. Wang, W. Cai, R. Chen, J. Gao, X. Yang, W. Chen, Y. Huang, H.M. Chen, C.M. Li, T. Zhang, B. Liu, Atomically dispersed Ni(i) as the active site for electrochemical CO_2 reduction, *Nat. Energy* 3 (2018) 140–147, <https://doi.org/10.1038/s41560-017-0078-8>.

[18] X. Li, W. Bi, M. Chen, Y. Sun, H. Ju, W. Yan, J. Zhu, X. Wu, W. Chu, C. Wu, Y. Xie, Exclusive Ni-N₄ sites realize near-unity CO selectivity for electrochemical CO_2 reduction, *J. Am. Chem. Soc.* 139 (2017) 14889–14892, <https://doi.org/10.1021/jacs.7b09074>.

[19] W. Ren, X. Tan, W. Yang, C. Jia, S. Xu, K. Wang, S.C. Smith, C. Zhao, Isolated diatomic Ni-Fe metal-nitrogen sites for synergistic electroreduction of CO_2 , *Angew. Chem. Int. Ed.* 58 (2019) 6972–6976, <https://doi.org/10.1002/anie.201901575>.

[20] J. Li, P. Pršlja, T. Shinagawa, A.J. Martín Fernández, F. Krumeich, K. Artushkova, P. Atanassov, A. Zitolo, Y. Zhou, R. García-Muelas, N. López, J. Pérez-Ramírez, F. Jaouen, Volcano trend in electrocatalytic CO_2 reduction activity over atomically dispersed metal sites on nitrogen-doped carbon, *ACS Catal.* 9 (2019) 10426–10439, <https://doi.org/10.1021/acscatal.9b02594>.

[21] C. Wang, X. Hu, X. Hu, X. Liu, Q. Guan, R. Hao, Y. Liu, W. Li, Typical transition metal single-atom catalysts with a metal-pyridine N structure for efficient CO_2 electroreduction, *Appl. Catal. B-Environ.* 296 (2021), 120331, <https://doi.org/10.1016/j.apcatb.2021.120331>.

[22] X.-M. Hu, H.H. Hval, E.T. Bjerglund, K.J. Dalggaard, M.R. Madsen, M.-M. Pohl, E. Welter, P. Lamagni, K.B. Buhl, M. Bremholm, M. Beller, S.U. Pedersen, T. Skrydstrup, K. Daabsberg, Selective CO_2 reduction to CO in water using earth-abundant metal and nitrogen-doped carbon electrocatalysts, *ACS Catal.* 8 (2018) 6255–6264, <https://doi.org/10.1021/acscatal.8b01022>.

[23] F. Pan, H. Zhang, K. Liu, D. Cullen, K. More, M. Wang, Z. Feng, G. Wang, G. Wu, Y. Li, Unveiling active sites of CO_2 reduction on nitrogen-coordinated and atomically dispersed iron and cobalt catalysts, *ACS Catal.* 8 (2018) 3116–3122, <https://doi.org/10.1021/acscatal.8b00398>.

[24] W. Bi, X. Li, R. You, M. Chen, R. Yuan, W. Huang, X. Wu, W. Chu, C. Wu, Y. Xie, Surface immobilization of transition metal ions on nitrogen-doped graphene realizing high-efficient and selective CO_2 reduction, *Adv. Mater.* 30 (2018), 1706617, <https://doi.org/10.1002/adma.201706617>.

[25] L. Takele Menisa, P. Cheng, C. Long, X. Qiu, Y. Zheng, J. Han, Y. Zhang, Y. Gao, Z. Tang, Insight into atomically dispersed porous M-N-C single-site catalysts for electrochemical CO_2 reduction, *Nanoscale* 12 (2020) 16617–16626, <https://doi.org/10.1039/d0nr03044a>.

[26] H.L. Jiang, L. Jiao, W. Yang, G. Wan, R. Zhang, X. Zheng, H. Zhou, S.H. Yu, Single-atom electrocatalysts from multivariate MOFs for highly selective reduction of CO_2 at low pressures, *Angew. Chem. Int. Ed.* (2020), <https://doi.org/10.1002/anie.202008787>.

[27] W. Zheng, F. Chen, Q. Zeng, Z. Li, B. Yang, L. Lei, Q. Zhang, F. He, X. Wu, Y. Hou, A. Universal, Principle to accurately synthesize atomically dispersed metal-N₄ sites for CO_2 electroreduction, *Nano-Micro Lett.* 12 (2020) 108, <https://doi.org/10.1007/s40820-020-00443-z>.

[28] H. Yang, Q. Lin, C. Zhang, X. Yu, Z. Cheng, G. Li, Q. Hu, X. Ren, Q. Zhang, J. Liu, C. He, Carbon dioxide electroreduction on single-atom nickel decorated carbon membranes with industry compatible current densities, *Nat. Commun.* 11 (2020) 593, <https://doi.org/10.1038/s41467-020-14402-0>.

[29] J. Feng, H. Gao, L. Zheng, Z. Chen, S. Zeng, C. Jiang, H. Dong, L. Liu, S. Zhang, X. Zhang, A Mn-N₃ single-atom catalyst embedded in graphitic carbon nitride for efficient CO_2 electroreduction, *Nat. Commun.* 11 (2020) 4341, <https://doi.org/10.1038/s41467-020-18143-y>.

[30] X. Xie, C. He, B. Li, Y. He, D.A. Cullen, E.C. Wegener, A.J. Kropf, U. Martinez, Y. Cheng, M.H. Engelhard, M.E. Bowden, M. Song, T. Lemmon, X.S. Li, Z. Nie, J. Liu, D.J. Myers, P. Zelenay, G. Wang, G. Wu, V. Ramani, Y. Shao, Performance enhancement and degradation mechanism identification of a single-atom Co-N-C catalyst for proton exchange membrane fuel cells, *Nat. Catal.* 3 (2020) 1044–1054, <https://doi.org/10.1038/s41929-020-00546-1>.

[31] D.M. Koshy, S. Chen, D.U. Lee, M.B. Stevens, A.M. Abdellah, S.M. Dull, G. Chen, D. Nordlund, A. Gallo, C. Hahn, D.C. Higgins, Z. Bao, T.F. Jaramillo, Understanding the Origin of Highly Selective CO_2 Electroreduction to CO on Ni,N-doped Carbon, *Catal. Angew. Chem. Int. Ed.* 59 (2020) 4043–4050, <https://doi.org/10.1002/anie.201912857>.

[32] L. Yang, D. Cheng, H. Xu, X. Zeng, X. Wan, J. Shui, Z. Xiang, D. Cao, Unveiling the high-activity origin of single-atom iron catalysts for oxygen reduction reaction, *P. Natl. Acad. Sci. USA* 115 (2018) 6626–6631, <https://doi.org/10.1073/pnas.1800771115>.

[33] Y. Mi, Y. Qiu, Y. Liu, X. Peng, M. Hu, S. Zhao, H. Cao, L. Zhuo, H. Li, J. Ren, X. Liu, J. Luo, Cobalt-iron oxide nanosheets for high-efficiency solar-driven CO_2 - H_2O coupling electrocatalytic reactions, *Adv. Funct. Mater.* 30 (2020), <https://doi.org/10.1002/adfm.202003438>.

[34] M. Schreier, F. Héroguel, L. Steier, S. Ahmad, J.S. Luterbacher, M.T. Mayer, J. Luo, M. Grätzel, Solar conversion of CO_2 to CO using earth-abundant electrocatalysts prepared by atomic layer modification of CuO, *Nat. Energy* 2 (2017), <https://doi.org/10.1038/nenergy.2017.87>.

[35] Z. Chen, T. Wang, B. Liu, D. Cheng, C. Hu, G. Zhang, W. Zhu, H. Wang, Z.J. Zhao, J. Gong, Grain-boundary-rich copper for efficient solar-driven electrochemical CO_2 reduction to ethylene and ethanol, *J. Am. Chem. Soc.* 142 (2020) 6878–6883, <https://doi.org/10.1021/jacs.0c00971>.

[36] G. Gurudayal, J. Bullock, D.F. Srankó, C.M. Towle, Y. Lum, M. Hettick, M.C. Scott, A. Javey, J. Ager, Efficient solar-driven electrochemical CO_2 reduction to hydrocarbons and oxygenates, *Energy Environ. Sci.* 10 (2017) 2222–2230, <https://doi.org/10.1039/c7ee01764b>.

[37] B. Hasa, M. Jouny, B.H. Ko, B. Xu, F. Jiao, Flow electrolyzer mass spectrometry with a gas-diffusion electrode design, *Angew. Chem. Int. Ed.* 60 (2021) 3277–3282, <https://doi.org/10.1002/anie.202013713>.

[38] T. Möller, W. Ju, A. Bagger, X. Wang, F. Luo, T. Ngo Thanh, A.S. Varela, J. Rossmeisl, P. Strasser, Efficient CO_2 to CO electrolysis on solid Ni-N-C catalysts at industrial current densities, *Energy Environ. Sci.* 12 (2019) 640–647, <https://doi.org/10.1039/c8ee02662a>.

[39] Z. Chen, X. Zhang, W. Liu, M. Jiao, K. Mou, X. Zhang, L. Liu, Amination strategy to boost the CO_2 electroreduction current density of M-N/C single-atom catalysts to the industrial application level, *Energy Environ. Sci.* 14 (2021) 2349–2356, <https://doi.org/10.1039/d0ee04052e>.

[40] H. Yang, L. Shang, Q. Zhang, R. Shi, G.I.N. Waterhouse, L. Gu, T. Zhang, A universal ligand mediated method for large scale synthesis of transition metal single atom catalysts, *Nat. Commun.* 10 (2019) 4585, <https://doi.org/10.1038/s41467-019-12510-0>.

[41] F. Pan, W. Deng, C. Justiniano, Y. Li, Identification of champion transition metals centers in metal and nitrogen-codoped carbon catalysts for CO_2 reduction, *Appl. Catal. B-Environ.* 226 (2018) 463–472, <https://doi.org/10.1016/j.apcatb.2018.01.001>.

[42] W.H. Lai, Z. Miao, Y.X. Wang, J.Z. Wang, S.L. Chou, Atomic-local environments of single-atom catalysts: synthesis, electronic structure, and activity, *Adv. Energy Mater.* 9 (2019), 1900722, <https://doi.org/10.1002/aenm.201900722>.

[43] L. Sun, Z. Huang, V. Reddu, T. Su, A.C. Fisher, X. Wang, A planar, conjugated N₄-macrocyclic cobalt complex for heterogeneous electrocatalytic CO_2 reduction with high activity, *Angew. Chem. Int. Ed.* 59 (2020) 17104–17109, <https://doi.org/10.1002/anie.202007445>.

[44] M. Li, S. Chen, Q. Jiang, Q. Chen, X. Wang, Y. Yan, J. Liu, C. Lv, W. Ding, X. Guo, Origin of the activity of Co-N-C catalysts for chemoselective hydrogenation of nitroarenes, *ACS Catal.* 11 (2021) 3026–3039, <https://pubs.acs.org/doi/10.1021/acscatal.0c05479>.

[45] W. Ju, A. Bagger, G.P. Hao, A.S. Varela, I. Sinev, V. Bon, B. Roldan Cuenya, S. Kaskel, J. Rossmeisl, P. Strasser, Understanding activity and selectivity of metal-nitrogen-doped carbon catalysts for electrochemical reduction of CO_2 , *Nat. Commun.* 8 (2017) 944, <https://doi.org/10.1038/s41467-017-01035-z>.

[46] W. Zhu, L. Zhang, S. Liu, A. Li, X. Yuan, C. Hu, G. Zhang, W. Deng, K. Zang, J. Luo, Y. Zhu, M. Gu, Z.J. Zhao, J. Gong, Enhanced CO_2 electroreduction on neighboring Zn/Co monomers by electronic effect, *Angew. Chem. Int. Ed.* 59 (2020) 12664–12668, <https://doi.org/10.1002/anie.201916218>.